Supplementary material

Redox induced controlling microporosity of zeolitic transition metal oxides based on ε-Keggin ironmolybdate in an ultra-fine level

Qingqing Liu, [a] Shufan Yao, [a] Denan Li, [a] Baokai Ma, [a] Tianyi Zhang, [a] Qianqian Zhu, [a] *

Dingbing He, [b] Masahiro Sadakane, [c] Yanshuo Li, [a, b] * Wataru Ueda, [d] and Zhenxin Zhang [a] *

[a] School of Materials Science and Chemical Engineering, Ningbo University, Fenghua Road 818, Ningbo, Zhejiang, 315211, P. R. China. E-mail: zhuqianqian@nbu.edu.cn (Q.Z.), zhangzhenxin@nbu.edu.cn (Z.Z.), liyanshuo@nbu.edu.cn (Y.L.)

[b] Zhejiang Hymater New Materials Co., Ltd. Ningbo, Zhejiang, 315034, P. R. China

[c] Department of Applied Chemistry, Hiroshima University, 1-4-1 Kagamiyama, Higashi Hiroshima 739-8527, Japan

[d] Faculty of Engineering, Kanagawa University; Rokkakubashi, Kanagawa-ku, Yokohama-shi, Kanagawa, 221-8686, Japan

Experimental section

1. Synthesis of Na-IM

Na-IM was synthesized according to the reported literature. [1] $Na_2MoO_4 \cdot 2H_2O$ (2.117 g, 8.75 mmol based on Mo) was dissolved in 26 mL of H_2O. Then metal Mo (0.15 g, 1.56 mmol) and Fe_3O_4 (0.192 g, 0.83 mmol) were added in sequence, followed by adding 6.1 mL of H_2SO_4 (9.1 wt%). The mixture was introduced into a 50 mL stainless-steel well sealed autoclave with a Teflon liner, and the autoclave was fixed in an oven with a mechanical rotation system. Hydrothermal synthesis was performed at 175 °C with tumbling (4.2 rpm) for 48 h. After the hydrothermal reaction and the autoclave had been cooled down, the crude solid was moved to a 100 mL beaker, and 60 mL of water was added. For purification and solid recovery, the resulting suspension (containing the product) was centrifuged (3900 rpm, 5 min), and the solids on the bottom of the centrifugation tube were collected. The unreacted Fe_3O_4 was removed by a magnet. After addition of 60 mL of H_2O to the remaining solids, the solution was centrifuged (1500 rpm, 2 min), and the upper suspension solution was obtained. After the process was repeated for three times, the obtained suspension was centrifuged (3900 rpm, 60 min). The solid on the bottom of the centrifugation tube was collected and dried under vacuum.

2. Characterization

Fourier transform infrared spectroscopy (FTIR) was performed on a Bruker Vertex 70. The testing pellet was prepared mixture KBr with the samples homogenously. Powder X-ray diffraction (XRD) patterns were obtained with a Bruker D8 Advance with Cu Kα radiation (tube voltage, 40 kV; tube current, 40 mA; scan speed, 8 °/min; 2θ range, 5-60°). X-ray photoelectron spectroscopy (XPS) was recorded on a Thermo Scientific K-Alpha. The spectrometer energies were calibrated using the C_{1s} peak at 284.8 eV. Thermogravimetry (TG) was carried out on a NETZSCH-STA 2500 Regulus. About 10 mg of dried samples under a N_2 flow of 20 mL/min with a heating rate of 10 °C/min from 20 °C to 600 °C.

3. Adsorption experiments

The materials were calcined at 200 °C for 2 h under a vacuum to remove the occupied H_2O in these materials before all adsorption experiments. Adsorption of CO_2 and CH_4 were separately carried out on the materials by a Micromeritics (3FLEX) sorption analyzer. Adsorption temperature was kept by at 0 °C and 25 °C, respectively. N_2 adsorption under high pressure was carried out on

Micromeritics (HPVAII-200) sorption analyze.

Adsorption enthalpy [2] and ideal adsorption solution theory (IAST) selectivity [3] calculation

In this paper, a dual-site Langmuir−Freundlich equation was used for medium temperature line fitting, adsorption enthalpy calculation and IAST fitting (**Figure S6**), given by

$$q = \frac{q_1 b_1 p^{n1}}{1 + b_1 p^{n1}} + \frac{q_2 b_2 p^{n2}}{1 + b_2 p^{n2}} \quad (1)$$

Where q is the adsorption capacity, p is the pressure, q_1, q_2, b_1, b_2, n_1, and n_2 are fitting parameters.

The resulting R^2 values of the fitting processes were quite close to 1, indicating that simulated isotherms by using the dual-site Langmuir–Freundlich model fitted the experimental isotherms well.

The adsorption enthalpies of CO_2 and CH_4 for the material were calculated by the Clausius-Clapeyron equation using the dual-site Langmuir-Freundlich fitting results (**Figure S8** and **Figure S9**) and the equation was as follows:

$$\frac{dlnp}{dT} = \frac{\Delta H}{RT^2} \quad (2)$$

Here p was pressure, T was temperature, and ΔH was enthalpy of adsorption.

4. Breakthrough measurement

The breakthrough measurements were performed in a self-made apparatus (**Figure S10**). The sample (1 g) was packed in a stainless-steel adsorption column with an inner diameter of 4.6 mm and a length of 50 mm to form an adsorbent bed. Before the breakthrough measurement, the adsorbent bed was heated under vacuum at 200 °C for 2 h, and cooled to room temperature. The gases with certain flow rates controlled by a flowmeter were mixed and introduced into the adsorbent bed at a certain temperature that was controlled with a water bath or an aluminum beads bath. In the case of the breakthrough measurement under humidity, water was introduced by bubbling and the content was controlled by temperature. The outlet composition was continuously monitored by gas chromatography (Agilent Technologies 7890B) with a thermal conductivity detector (GC-TCD) until the two gases reached equilibrium. Before the cycle breakthrough experiment, the material was heated at 200 °C vacuum for 2 h to remove the adsorbed gas molecules for regeneration.

The water content (percentage) was calculated to show the different water contents in different conditions. The water content was estimated again by the following equation:

$$water\ content = \frac{p_{water}}{p_{total}} \times 100\% \quad (3)$$

where p_{water} is saturated water vapor pressure at a certain temperature, p_{total} is the total pressure of the separation column during the breakthrough measurement measured by a pressure sensor, and p_{total} of the breakthrough measurements with humidity is 110 kPa.

Breakthrough selectivity

CO_2/CH_4 selectivity for **Na-IM**s was defined, the values were calculated by the equation:

$$s_{A/B} = \frac{x_A/y_A}{x_B/y_B} \quad (4)$$

Where x_A is the adsorption capacity of the final breakthrough gas (mmol/g), x_B is the adsorption capacity of the first breakthrough gas (mmol/g), y_A and y_B are the mole fractions of gas A and gas B in the mixture of gases, respectively.

The adsorption capacity of the gas i (i = A, B) was calculated by the equation:

$$x_i = \frac{V}{22.4 \times m} \times \int_0^t \left(1 - \frac{C(t)}{C_0(t)}\right) dt \quad (5)$$

where V is flow rate of gas i (mL/min), t is the adsorption time (min), C and C_0 are the inlet and outlet gas molar flow rates, respectively, and m is the mass of the sample (g).

5. Structure modeling and the DFT calculation

The primitive cell was used for DFT calculation. Static binding energy and transition state energy were conducted on Density functional theory (DFT) calculations. Optimizing the structures of the materials was carried out with Vienna Ab initio Simulation Package (VASP). [4, 5] The PBE exchange-correlation functional based on generalized gradient approximation was employed. [6] The Plane wave basis sets used to approximate wave functions of valence electrons were included to a 400 eV kinetic energy cut-off. The projector-augmented wave (PAW) method was adopted to describe interactions between valence electrons and atom cores. [7] All calculations were spin-polarized. Gaussian smearing with a width of 0.1 eV was imposed for electron distributions near the Fermi Level. The electronic structures and geometries of structures were optimized until the

energy differences between successive steps were less than 1×10^{-4} eV and 1×10^{-3} eV respectively. For modeling the dispersion interactions, the DFT-D3 method was adopted. [8] The primitive cell used for simulation contains two ε-Keggin units. The 1×1 unit cell with a corresponding $3 \times 3 \times 3$ Gamma k-point mesh generated by post-processing VASPKIT package was used. [9, 10]

Complete linear synchronous transit (LST) method was adopted to generate an initial pathway of gas molecules passing through the unit cell. [11] The diffusion barrier energies were obtained with climbing image nudged elastic band (cNEB). [12, 13]

Static binding energy calculation that predicted the interaction of the gas molecule and the solid material. Generally, the formation energy is given by

$$E_s = E_{(material)} + E_{(molecule)} - E_{(material\ +\ molecule)} \quad (6)$$

where E_s is the static binding energy, $E_{(material)}$ is the energy of the material, $E_{(molecule)}$ is the energy of the molecule, and $E_{(material + molecule)}$ is the energy of the material with the adsorbed molecule.

Activation energy calculation that predicted the energy difference between the transition state and the energy of the system with molecule in the cavity.

$$\Delta E_t = E_{ts} - E_{(material + molecule)} \quad (7)$$

where ΔE_t is the activation energy, E_{ts} is the energy of transition state, and $E_{(material + molecule)}$ is the energy of the material with the adsorbed molecule.

Structure modeling, average aperture size estimation, and pore volume estimation were performed with the Materials Studio package (Accelrys Software Inc.). The values of unit cell volume are directly calculated by the Materials Studio software package with the program of "atom volumes & surfaces". The values of average aperture are calculated by the equation:

$$\text{average aperture} = \bar{\varphi} - d_O, \quad (8)$$

where $\bar{\varphi}$ is the average distance of O in the pore opening in a single cell, which was measured in the Materials Studio software; d_O is diameter of oxygen atom (2.92 Å). [14]

The values of pore volume are calculated by the equation:

$$\text{pore volume} = \text{free volume} \times \frac{N_A \times 10^{-24}}{M(H_{18}O_{80}Fe_6Mo_{24})} \quad (9)$$

where N_A is Avogadro constant, M is molar mass of the material with the formula of $H_{18}O_{80}Fe_6Mo_{24}$, and free volume was obtained by the Materials Studio software package with the program of "atom volumes & surfaces, Connolly surface, and ultra-fine".

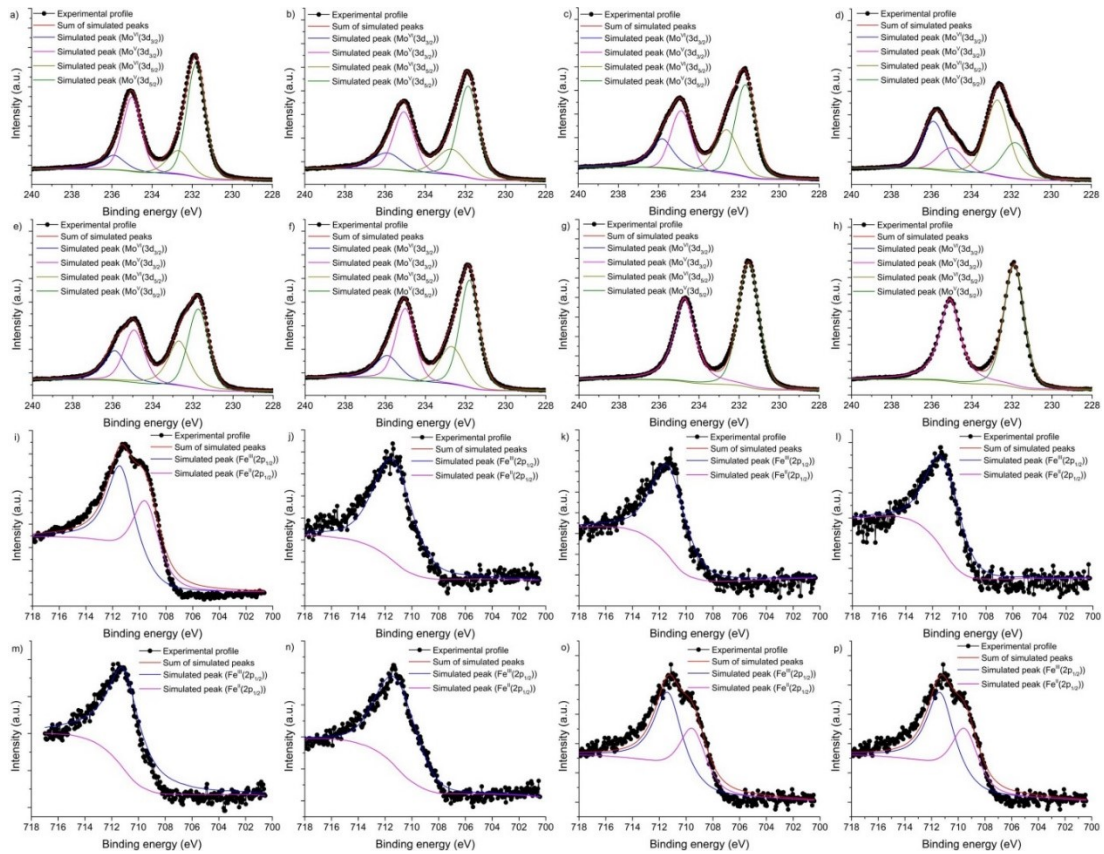

Figure S1. XPS profiles of Mo in a) Mo in **Na-IM**, b) Mo in **Na-IMAC40**, c) Mo in **Na-IMAC80**, d) Mo in **Na-IMAC150**, e) Mo in **Na-IMRe0.003**, f) Mo in **Na-IMRe0.03**, g) Mo in **Na-IMRe0.1**, h) Mo in **Na-IMRe0.3**, i) Fe in **Na-IM**, j) Fe in **Na-IMAC40**, k) Fe in **Na-IMAC80**, l) Fe in **Na-IMAC150**, m) Fe in **Na-IMRe0.003**, n) Fe in **Na-IMRe0.03**, o) Fe in **Na-IMRe0.1**, and p) Fe in **Na-IMRe0.3**.

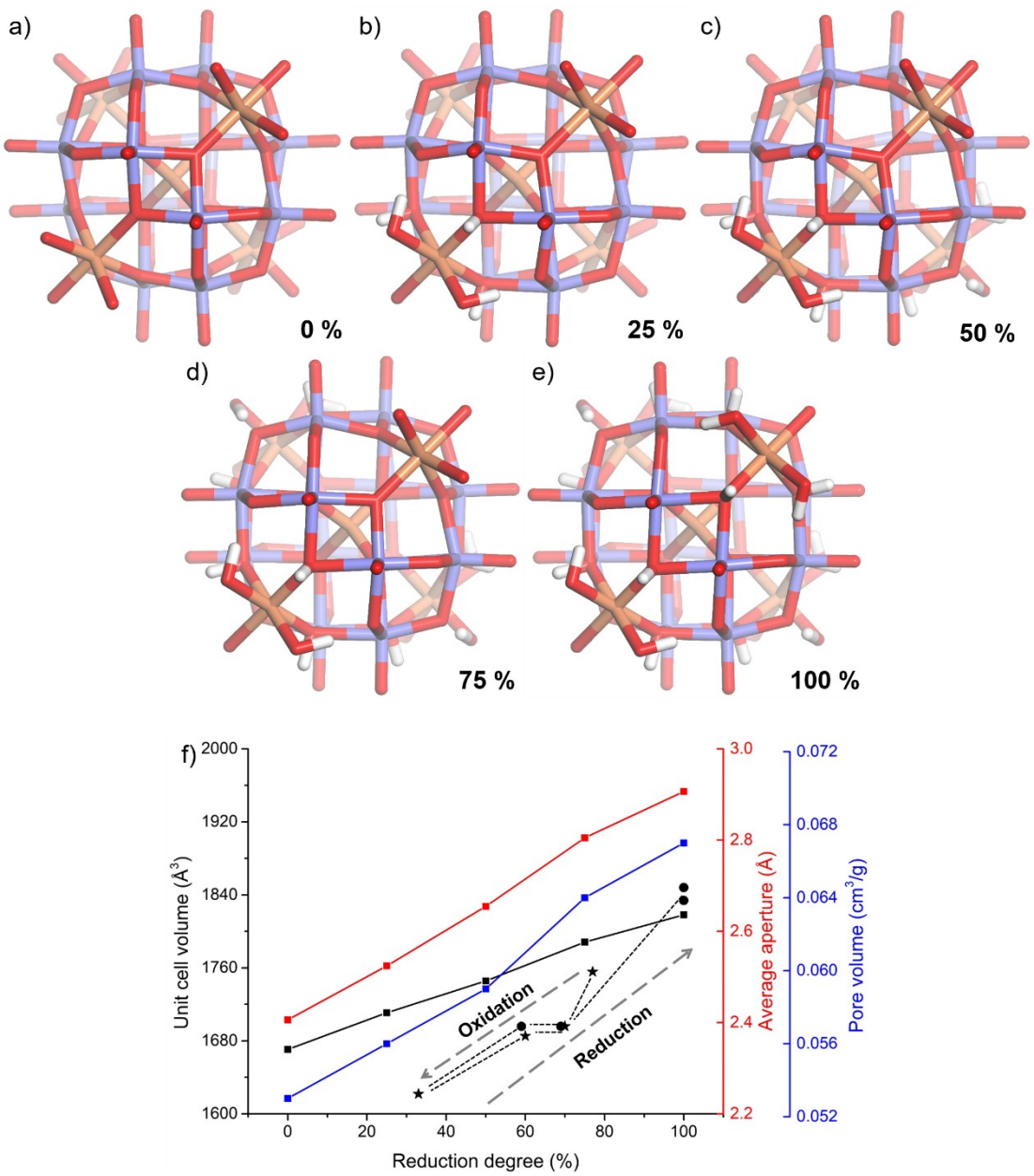

Figure S2. Structure models of *ε*-Keggin POM unit of **Na-IM** with the reduction degrees of a) 0%, b) 25%, c) 50%, d) 75%, and e) 100% and f) corresponding theoretical (black solid line) and experimental (black dash line) unit cell volume, average pore volume (red solid line), and pore volume (blue solid line) changes with reduction degree, Mo (lilac), Fe (orange), O (red), H (white).

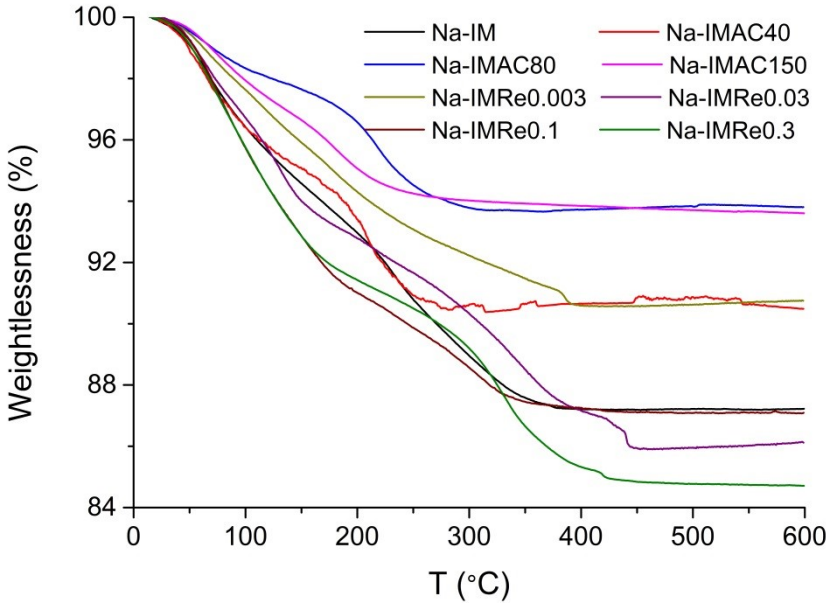

Figure S3. TG curve of **Na-IM**, **Na-IMAC40**, **Na-IMAC80**, **Na-IMAC150**, **Na-IMRe0.003**, **Na-IMRe0.03**, **Na-IMRe0.1**, and **Na-IMRe0.3**.

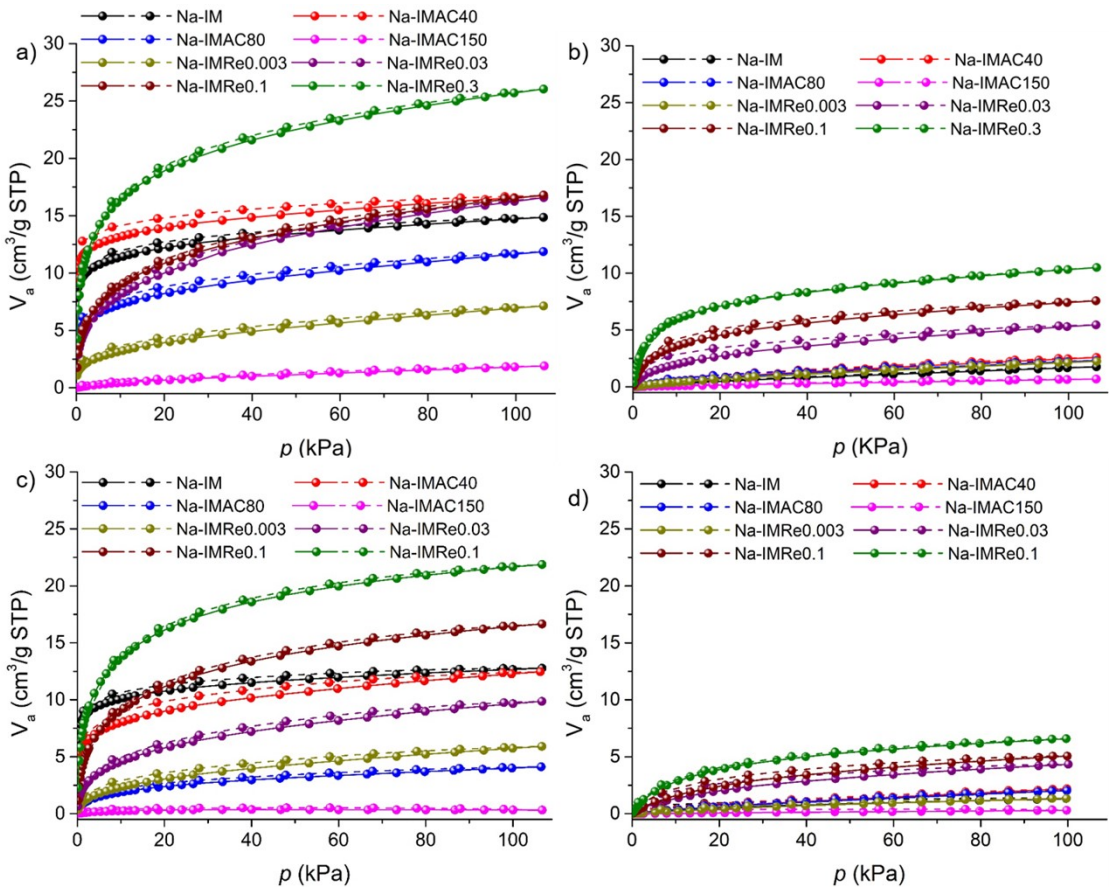

Figure S4. a) CO_2 and b) CH_4 adsorption (solid line)-desorption (dash line) isotherms of **Na-IM**, **Na-IMAC40**, **Na-IMAC80**, **Na-IMAC150**, **Na-IMRe0.003**, **Na-IMRe0.03**, **Na-IMRe0.1**, and **Na-IMRe0.3** at 0 °C. c) CO_2 and d) CH_4 adsorption (solid line)-desorption (dash line) isotherms of **Na-IM**, **Na-IMAC40**, **Na-IMAC80**, **Na-IMAC150**, **Na-IMRe0.003**, **Na-IMRe0.03**, **Na-IMRe0.1**, and **Na-IMRe0.3** at 25 °C.

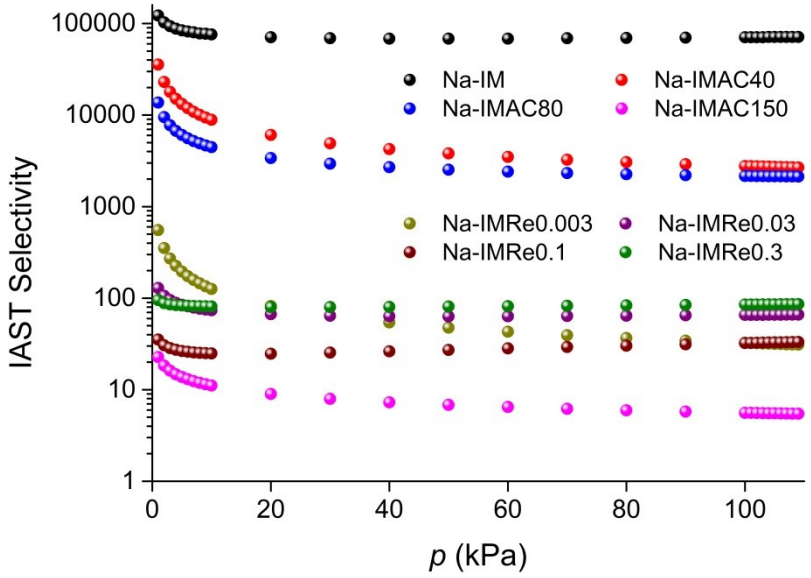

Figure S5. IAST selectivity of CO_2/CH_4 with the ratio of 1/1 (v/v) for **Na-IM**s

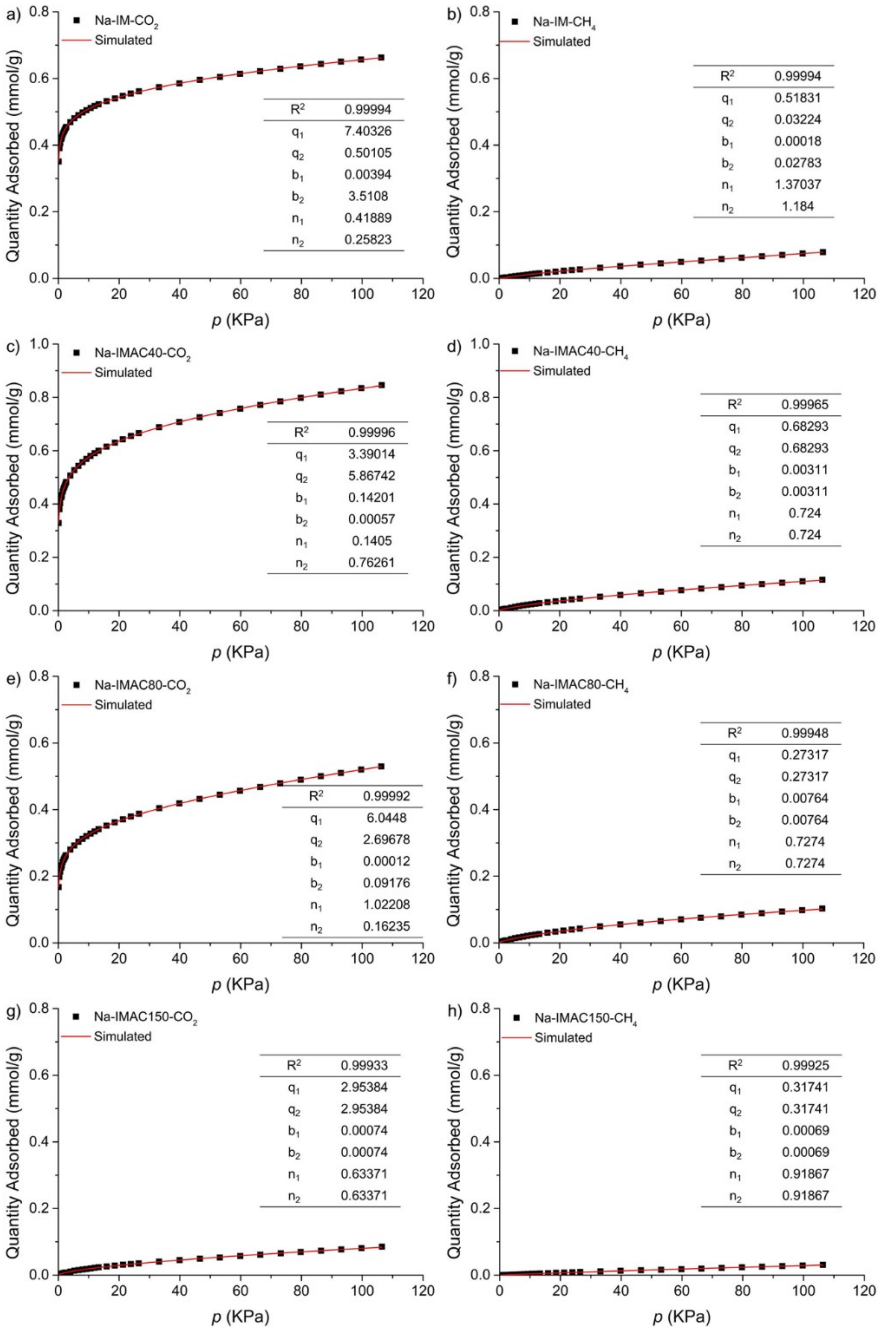
a)
Na-IM-CO2
Simulated
R2 0.99994
q1 7.40326
q2 0.50105
b1 0.00394
b2 3.5108
n1 0.41889
n2 0.25823
b)
Na-IM-CH4
Simulated
R2 0.99994
q1 0.51831
q2 0.03224
b1 0.00018
b2 0.02783
n1 1.37037
n2 1.184
c)
Na-IMAC40-CO2
Simulated
R2 0.99996
q1 3.39014
q2 5.86742
b1 0.14201
b2 0.00057
n1 0.1405
n2 0.76261
d)
Na-IMAC40-CH4
Simulated
R2 0.99965
q1 0.68293
q2 0.68293
b1 0.00311
b2 0.00311
n1 0.724
n2 0.724
e)
Na-IMAC80-CO2
Simulated
R2 0.99992
q1 6.0448
q2 2.69678
b1 0.00012
b2 0.09176
n1 1.02208
n2 0.16235
f)
Na-IMAC80-CH4
Simulated
R2 0.99948
q1 0.27317
q2 0.27317
b1 0.00764
b2 0.00764
n1 0.7274
n2 0.7274
g)
Na-IMAC150-CO2
Simulated
R2 0.99933
q1 2.95384
q2 2.95384
b1 0.00074
b2 0.00074
n1 0.63371
n2 0.63371
h)
Na-IMAC150-CH4
Simulated
R2 0.99925
q1 0.31741
q2 0.31741
b1 0.00069
b2 0.00069
n1 0.91867
n2 0.91867
Quantity Adsorbed (mmol/g)
p (KPa)

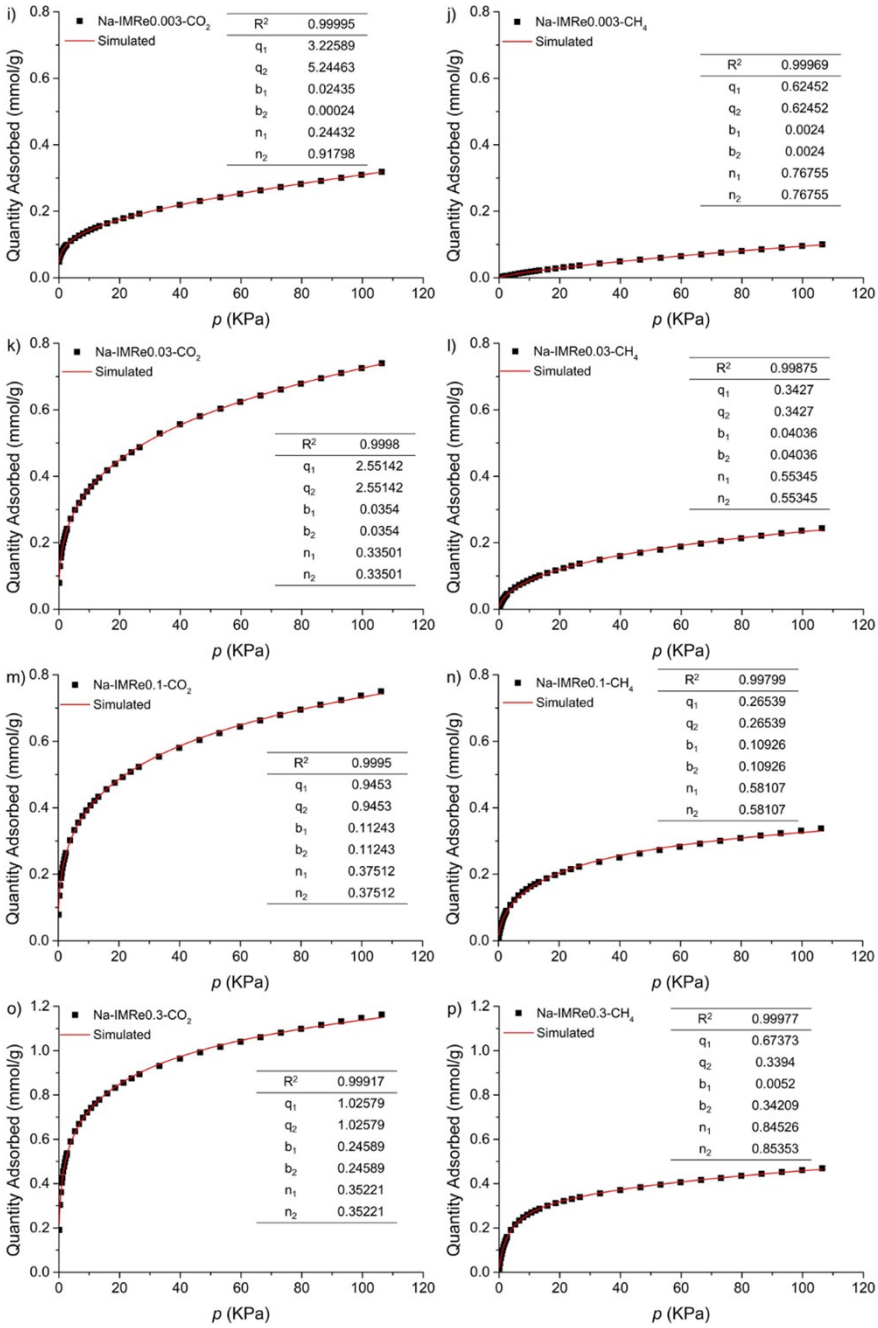

Figure S6. CO_2 and CH_4 adsorption isotherms and the fitting with the dual-site Langmuir-Freundlich model for the IAST selectivity calculation, a) CO_2 adsorption of **Na-IM**, b) CH_4 adsorption of **Na-IM**, c) CO_2 adsorption of **Na-IMAC40**, d) CH_4 adsorption of **Na-IMAC40**, e) CO_2 adsorption of **Na-IMAC80**, f) CH_4 adsorption of **Na-IMAC80**, g) CO_2 adsorption of **Na-IMAC150**, h) CH_4 adsorption of **Na-IMAC150**, i) CO_2 adsorption of **Na-IMRe0.003**, j) CH_4 adsorption of **Na-IMRe0.003**, k) CO_2 adsorption of **Na-IMRe0.03**, l) CH_4 adsorption of **Na-IMRe0.03**, m) CO_2 adsorption of **Na-IMRe0.1**, n) CH_4 adsorption of **Na-IMRe0.1**, o) CO_2 adsorption of **Na-IMRe0.3**, and p) CH_4 adsorption of **Na-IMRe0.3** at 0 ^oC.

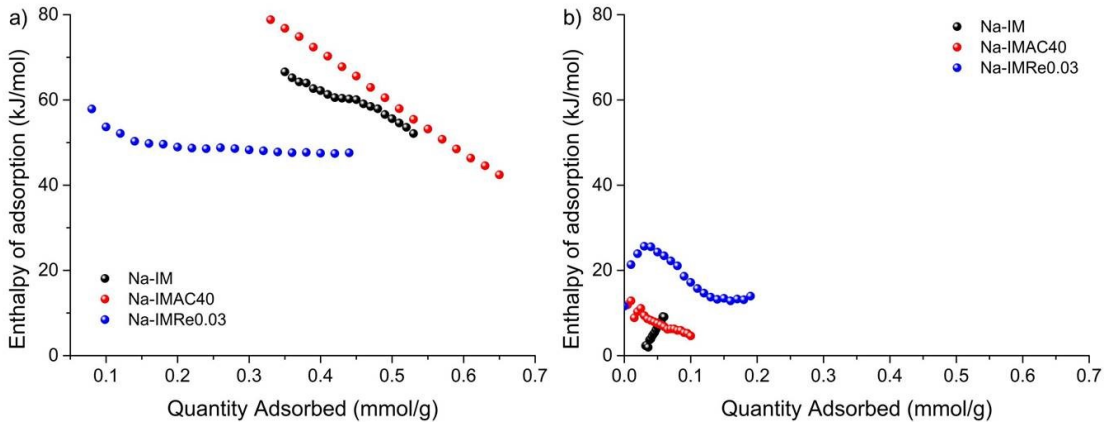

Figure S7. Adsorption enthalpy of a) CO_2 and b) CH_4 for **Na-IM**, **Na-IMAC40**, and **Na-IMRe0.03**.

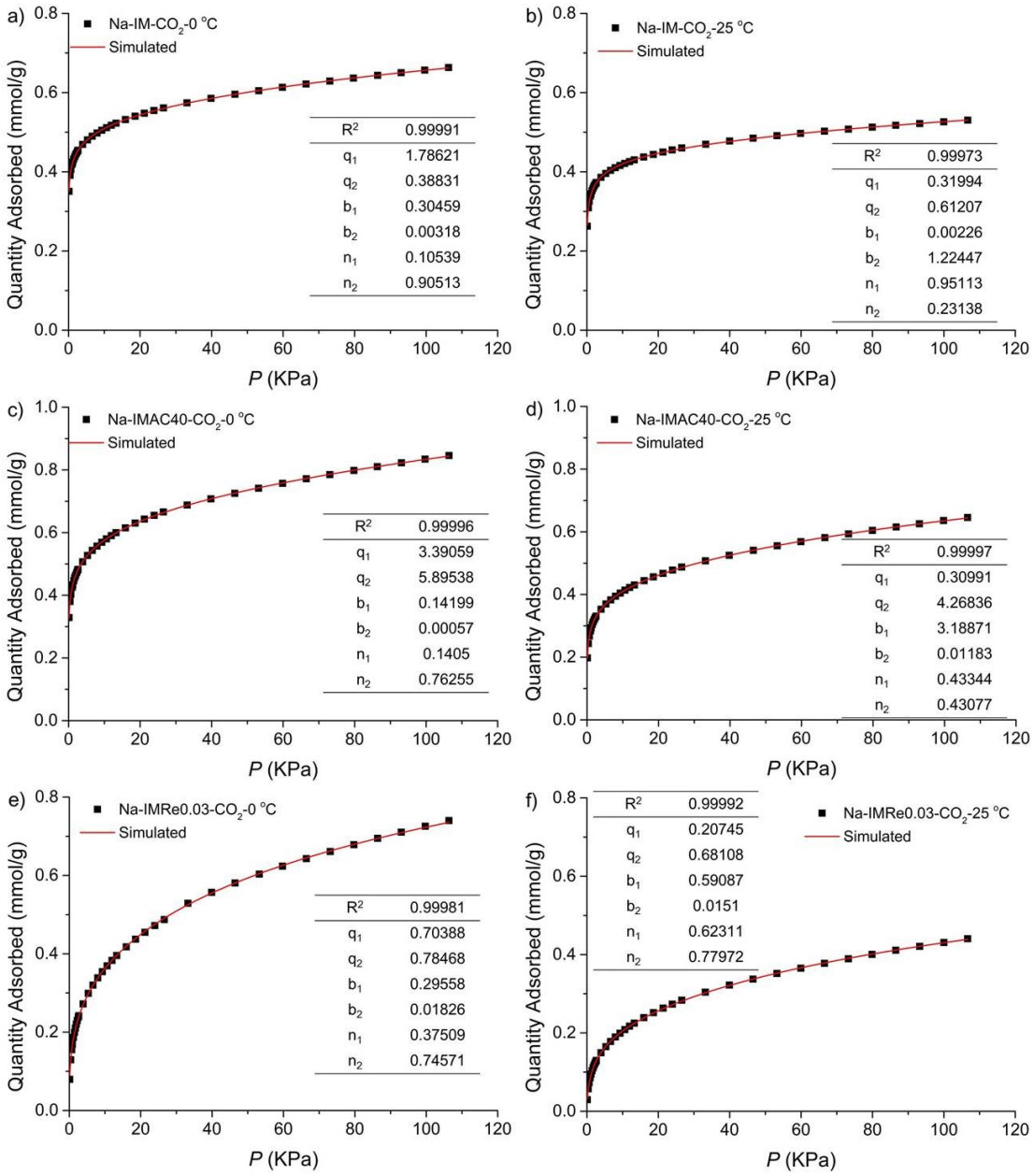

Figure S8. CO_2 adsorption isotherms and the fitting with the dual-site Langmuir-Freundlich model for the adsorption enthalpy calculation, a) **Na-IM** at 0 °C, b) **Na-IM** at 25 °C, c) **Na-IMAC40** at 0 °C, d) **Na-IMAC40** at 25 °C, e) **Na-IMRe0.03** at 0 °C, and f) **Na-IMRe0.03** at 25 °C.

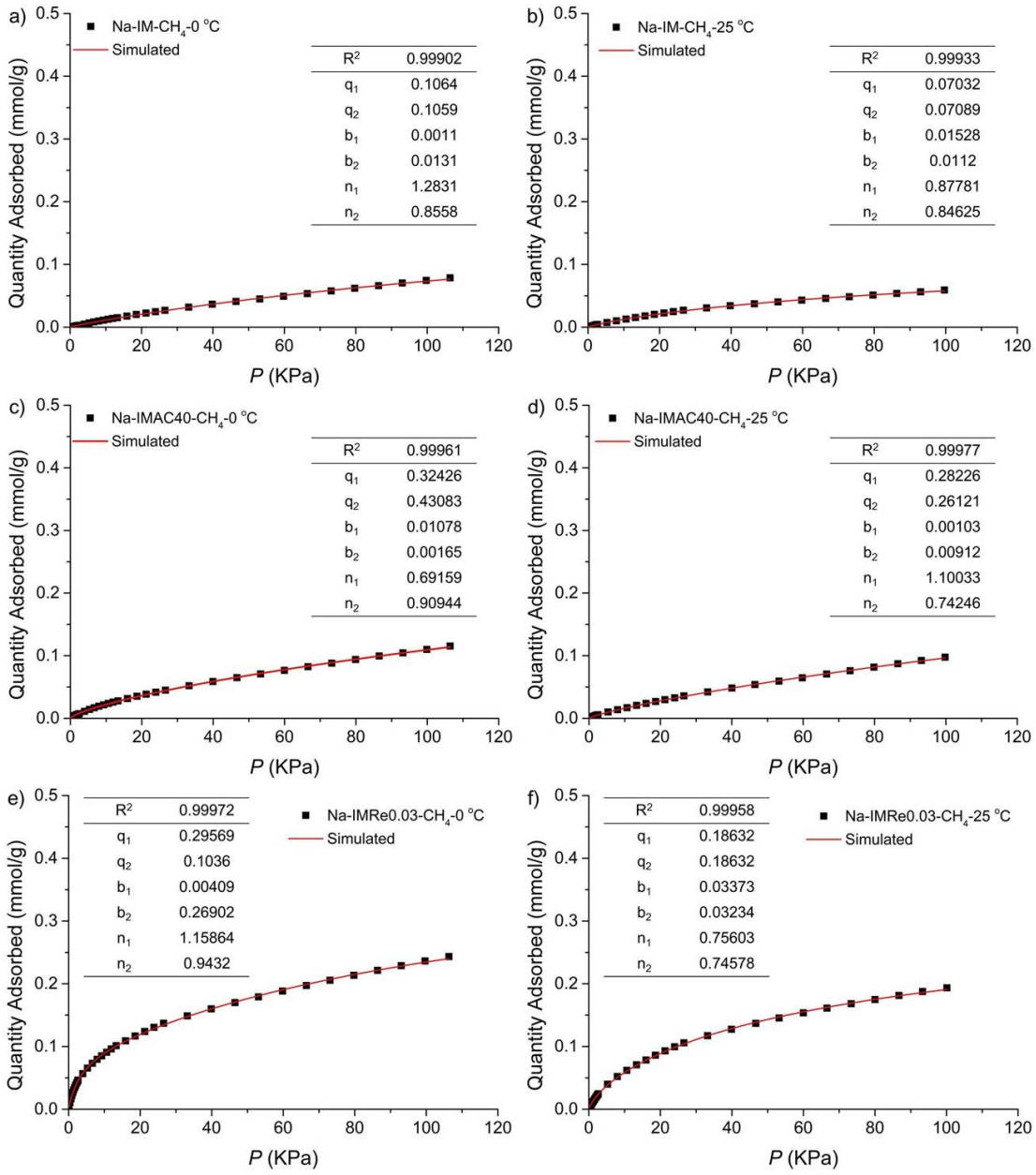

Figure S9. CH_4 adsorption isotherms and the fitting with the dual-site Langmuir-Freundlich model for the adsorption enthalpy calculation, a) **Na-IM** at 0 °C, b) **Na-IM** at 25 °C, c) **Na-IMAC40** at 0 °C, d) **Na-IMAC40** at 25 °C, e) **Na-IMRe0.03** at 0 °C, and f) **Na-IMRe0.03** at 25 °C.

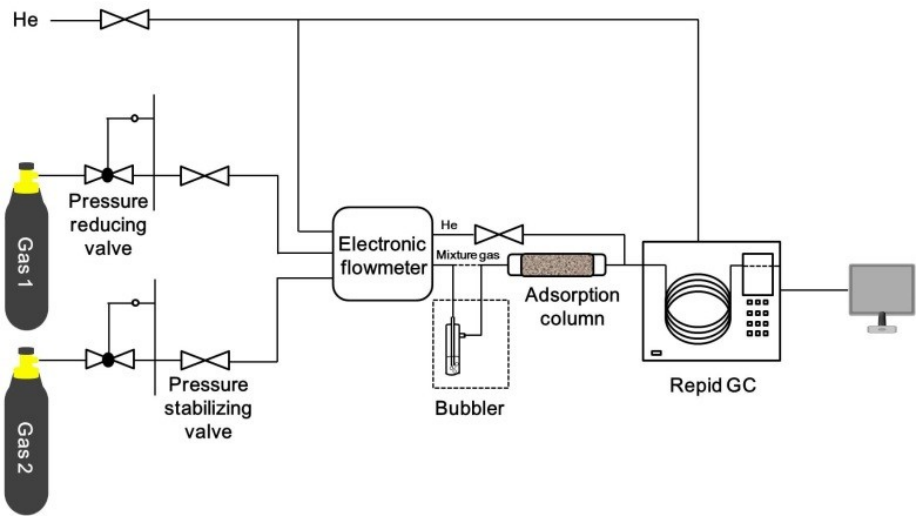

Figure S10. Schematic figure of the instrument for the breakthrough measurements.

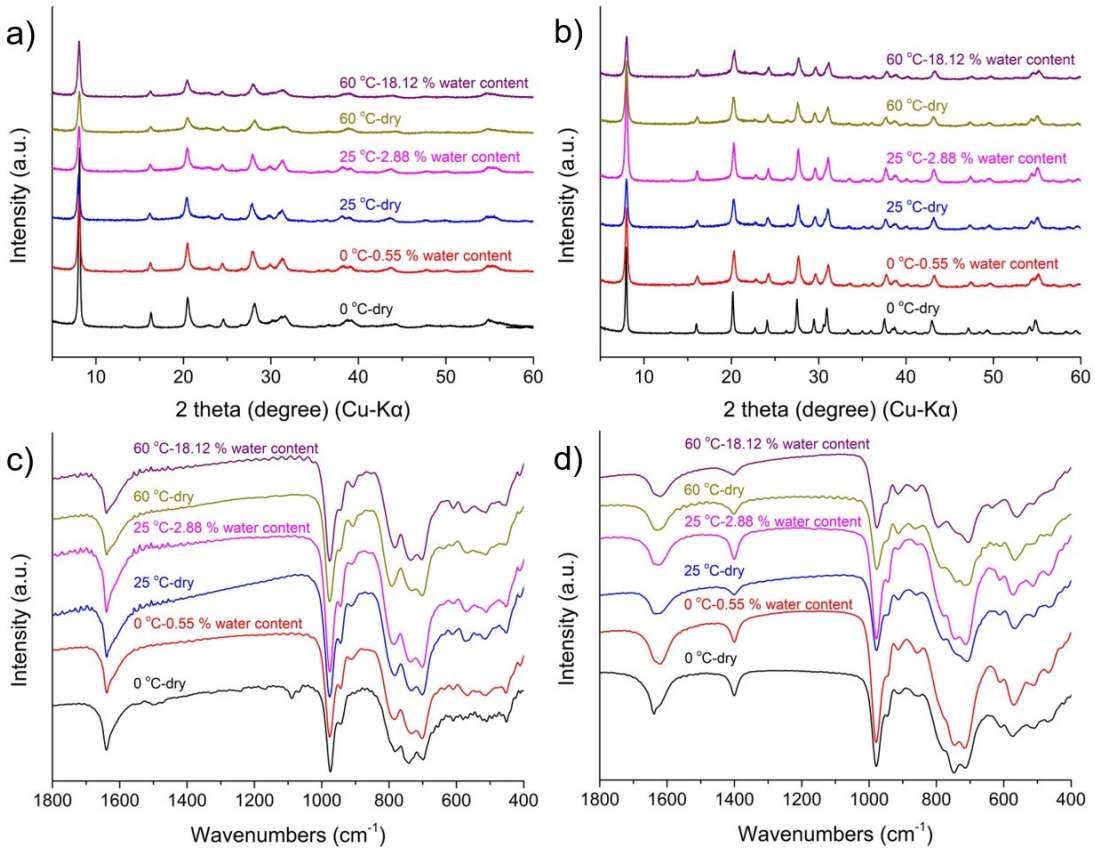

Figure S11. XRD patterns of a) **Na-IMAC40** and b) **Na-IMRe0.3** and FTIR spectra of c) **Na-IMAC40** and d) **Na-IMRe0.3** after the breakthrough measurements under different conditions.

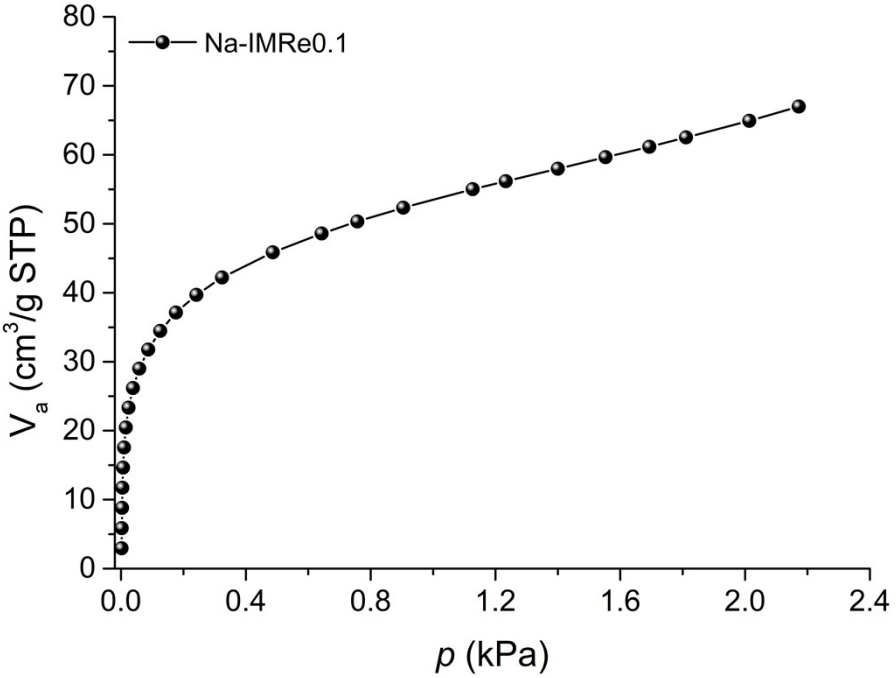

Figure S12. The water vapor adsorption of **Na-IMRe0.1**.

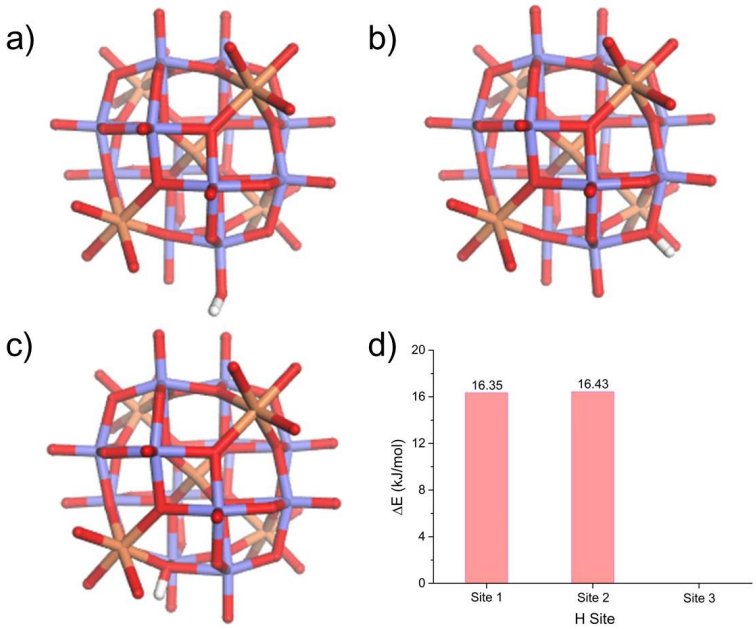

Figure S13. Structure models of ε-Keggin POM unit with different H sites, a) H in Site 1, b) H in Site 2, c) H in Site 3, and d) corresponding system energies with different H sites. Mo (lilac), Fe (orange), O (red), H (white).

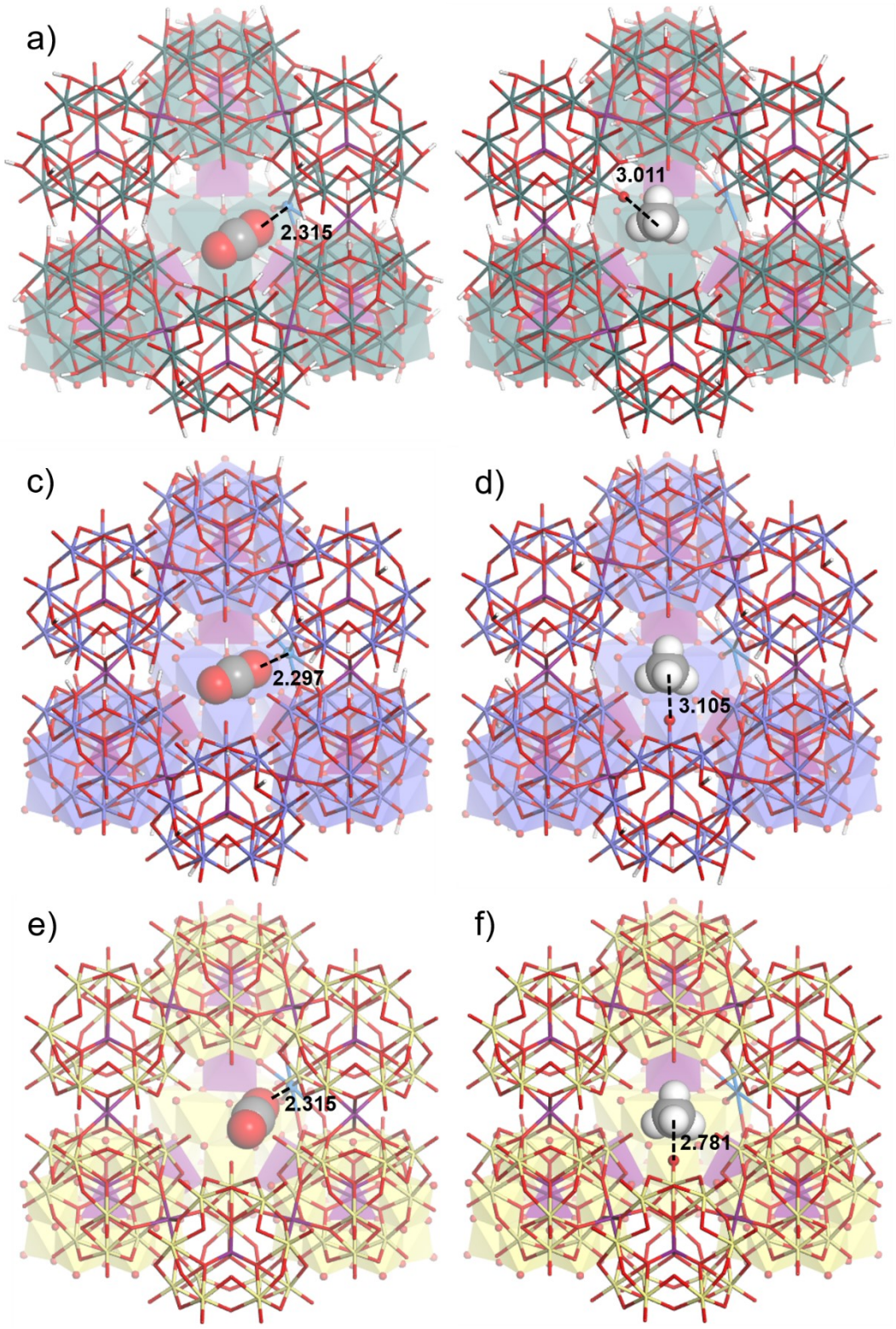

Figure S14. Structural models of **Na-IM** with different reduction degree. a) CO_2 and b) CH_4 in the cavity of **Na-IM** with100% reduction degree. c) CO_2 and d) CH_4 in the cavity of **Na-IM** with 50% reduction degree. e) CO_2 and f) CH_4 in the cavity of **Na-IM** with 0% reduction degree, Mo (green, lilac, and yellow), Fe (purple), O (red), H (white), C (grey), Na (blue).

Table S1. Valence of Mo and Fe and reduction degree for **Na-IM**s.

Materials	Mo^{V} : Mo^{VI}	Fe^{III} : Fe^{II}	Reduction degree (%) (Based on Mo)
Na-IM	3.28	1.28	77
Na-IMAC40	2.34	∞	70
Na-IMAC80	1.5	∞	60
Na-IMAC150	0.49	∞	33
Na-IMRe0.003	1.45	∞	59
Na-IMRe0.03	2.25	∞	69
Na-IMRe0.1	∞	1.45	100
Na-IMRe0.3	∞	1.25	100

Table S2. Microporosity of **Na-IM**s with different reduction degrees

Material	Reduction degree/% (Based Mo)	Limiting micropore volume/cm^3 STP g^{-1} (CO_2)	Limiting micropore volume/cm^3 STP g^{-1} (CH_4)	maximum adsorption capacity/cm^3 g^{-1} (CO_2)	maximum adsorption capacity/cm^3 g^{-1} (CH_4)	Pore volume/cm^3 g^{-1} (N_2)	Pore size/Å	BET surface area /cm^2 g^{-1}	The number of CO_2 in a cage	The number of CH_4 in a cage
Na-IM	77	0.0283	0.0066	14.85	1.76	0.0141	5.89	33.9	1.208	0.157
Na-IMAC40	70	0.0320	0.0072	16.74	1.72	0.0138	5.93	33.4	1.508	0.154
Na-IMAC80	60	0.0223	0.0067	12.48	1.81	0.0134	6.07	32.2	1.111	0.161
Na-IMAC150	33	0.0028	0.0028	1.90	0.69	0.0098	6.51	23.8	0.169	0.061
Na-IMRe0.003	59	0.0112	0.0047	7.14	2.25	0.0141	6.10	33.9	0.635	0.200
Na-IMRe0.03	69	0.0287	0.0118	16.58	5.45	0.0352	3.87	84.6	1.476	0.485
Na-IMRe0.1	100	0.0313	0.0177	16.80	7.57	0.0341	3.94	81.8	1.496	0.674
Na-IMRe0.3	100	0.0504	0.0250	26.05	10.50	0.0210	5.26	50.7	2.319	0.935

The values of the number of gases in a cage were calculated by the equation:

$$\text{the number of gases in a cage} = \frac{\text{adsorbed amount } (\text{cm}^3/\text{g}) \times \text{molecule weight of the material (g/mol)}}{22400\ (\text{cm}^3/\text{mol})}$$

Table S3. Separation performance of CO_2/CH_4 for **Na-IM**s with different reduction degrees.

Material	Reduction degree (%) (Based Mo)	Breakthrough selectivity	Δt_b (min)
Na-IM	77	25.7	37
Na-IMAC40	70	21.4	35
Na-IMAC80	60	35.0	34
Na-IMAC150	33	2.6	4
Na-IMRe0.003	59	4.3	7
Na-IMRe0.03	69	8.6	65
Na-IMRe0.1	100	18.6	62
Na-IMRe0.3	100	31.8	60

References

1. Q. Zhu, S. Yin, M. Zhou, J. Wang, C. Chen, P. Hu, X. Jiang, Z. Zhang, Y. Li and W. Ueda Aerobic alcohol oxidation by a zeolitic octahedral metal oxide based on iron vanadomolybdates under mild conditions, *ChemCatChem*, 2021, **13**, 1763-1771.
2. Z. Zhang, M. Sadakane, S. Noro, T. Murayama, T. Kamachi, K. Yoshizawa and W. Ueda, Selective carbon dioxide adsorption of ε-Keggin-type zincomolybdate-based purely-Inorganic 3D frameworks, *J. Mater. Chem. A*, 2015, **3**, 746-755.
3. A. L. Myers and J. M. Prausnitz, Thermodynamics of mixed-gas adsorption, *Aiche J.*, 1965, **11**, 121-127.
4. G. Kresse, Ab-Initio Molecular-Dynamics for Liquid-Metals, *J. Non-Cryst. Solids*, 1995, **193**, 222-229.
5. G. Kresse and J. Hafner, Ab initio molecular dynamics for liquid metals, *Phys. Rev. B Condens. Matter.*, 1993, **47**, 558-561.
6. J. P. Perdew, K. Burke and M. Ernzerhof, Generalized gradient approximation made simple, *Phys. Rev. Lett.*, 1996, **77**, 3865-3868.
7. P. E. Blöchl, Projector augmented-wave method, *Phys. Rev. B*, 1994, **50**, 17953.
8. S. Grimme, J. Antony, S. Ehrlich and H. Krieg, A consistent and accurate ab initio parametrization of density functional dispersion correction (DFT-D) for the 94 elements H-Pu, *J. Chem. Phys.*, 2010, **132**, 154104.
9. V. Wang, N. Xu, J. Liu, G. Tang, W. Geng, VASPKIT: A user-friendly interface facilitating high-throughput computing and analysis using VASP code, *Comput. Phys. Commun.*, 2021, **267**, 108033.
10. C. Hu, Heat-current operator and transport entropy of vortices in type-II superconductors, *Phys. Rev. B*, 1976, **13**, 4780-4783.
11. T. A. Halgren and W. N. Lipscomb, The synchronous-transit method for determining reaction pathways and locating molecular transition states, *Chem. Phys. Lett.*, 1977, **49**, 225-232.
12. G. Henkelman, B. P. Uberuaga and H. Jonsson, A climbing image nudged elastic band method for finding saddle points and minimum energy paths, *J. Chem. Phys.*, 2000, **113**, 9901-9904.
13. G. Henkelman and H. Jonsson, Improved tangent estimate in the nudged elastic band method for finding minimum energy paths and saddle points, *J. Chem. Phys.*, 2000, **113**, 9978-9985.
14. J. Tsai, R. Taylor, C. Chothia, and M. Gerstein, The Packing Density in Proteins: Standard Radii and Volumes, *J. Mol. Biol.*, 1999, **290**, 253-266.